

# Monochromatic Carbon Nanotube Tangles Grown by Microfluidic Switching between Chaos and Fractals

Zhenxing Zhu,<sup>II</sup> Nan Wei,<sup>II</sup> Bowen Yan, Boyuan Shen, Jun Gao, Silei Sun, Huanhuan Xie, Hao Xiong, Chenxi Zhang, Rufan Zhang, Weizhong Qian, Song Fu, Lianmao Peng, and Fei Wei\*



Cite This: *ACS Nano* 2021, 15, 5129–5137



Read Online

ACCESS |

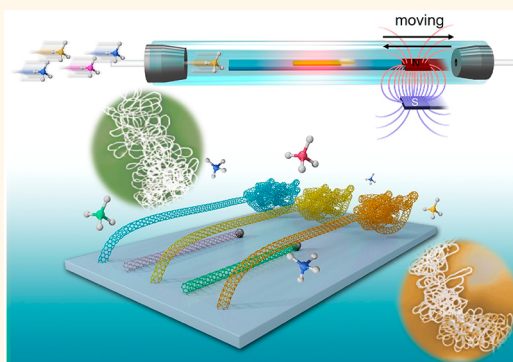
Metrics & More

Article Recommendations

Supporting Information

**ABSTRACT:** The nature of chaos is in that elusive flow that is an advanced order out of our vision. It is wise to take advantage of chaos after recognizing or modifying its unique fractal properties. Here, a magnetron weaving strategy was developed for producing chaotic but monochromatic carbon nanotube tangles (CNT-Ts) under Kelvin–Helmholtz instability (KHI). The self-similarity characteristic facilitated individual ultralong CNTs to manipulate their entropy-driven fractal geometry, resulting in  $\sim 10^4 \mu\text{m}^2$  CNT-Ts with variable curvature radius. In addition, based on the rate-selected mechanism, 85% metallic and  $\sim 100\%$  semiconducting CNT-Ts were synthesized and separated simultaneously at different length positions. After *ex situ* modifying their fractal into aligned CNTs with hydrogel, these CNT-Ts delivered a current of  $10 \mu\text{A} \mu\text{m}^{-1}$  in transistors with an on/off ratio  $> 10^7$ . It has provided the third route as a paradigm of applying one-dimensional nanomaterials by switching between chaos and fractal, in parallel with that of direct synthesis and postseparation.

**KEYWORDS:** ultralong carbon nanotubes, self-assembly, electronic devices, selective synthesis, fractal and chaos



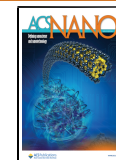
The theory of chaos and fractal is the art and science by which the structure and properties of matter in nature are made use of in fabricated parts and functional components.<sup>1,2</sup> It has been exemplified in stretched branches of trees, distributed blood vessels of heart, interfacial disordering of alloys, etc.<sup>3–5</sup> These physiological or crystalline systems appear chaotic, but actually, they are guided by definite fractal rules so as to resist volatility from the environment.<sup>1,6</sup> Three progressive aspects have dominated the principle of fractal in chaotic systems. The first is the minimum resistance that everything prefers to go through throughout its entire lifecycle. Second, the path of minimum resistance will be indicated by some potential and invisible structures. And third, these potential structures can generally be discovered or altered. Vibrant frameworks of chaos have endowed matters with high adaptability and flexibility due to their features of complexity, variability, and probability to smartly switch between different states.<sup>7</sup> For example, carbon nanotubes (CNTs) are the matter that holds great promise in next-generation electrical applications due to their exceptional properties.<sup>8,9</sup> They can be categorized into three material systems based on fractal geometry, including the agglomerated, vertically aligned, and horizontally aligned CNTs.<sup>10</sup> The

agglomerated CNTs possess the strongest mutual interaction, resulting in the thickest diameter, shortest length, and random orientations. By reducing their interaction, the morphology of CNTs with vertical alignment will be preferentially produced. But there still exists curling among CNTs, causing strong van der Waals interaction and large steric effects. When there is no interaction at all, the CNTs follow the tip-growth mode<sup>11</sup> and possess the largest intertube distance, leading to horizontally aligned ultralong CNTs with the lowest defect density.<sup>12</sup> They have been considered the optimal alternative to work as the channel material for high-end precise electronics,<sup>13,14</sup> whereas their controlled synthesis or manipulation has brought marked challenges as such an orderly fractal possesses the lowest configurational entropy.

Received: December 9, 2020

Accepted: January 12, 2021

Published: January 15, 2021



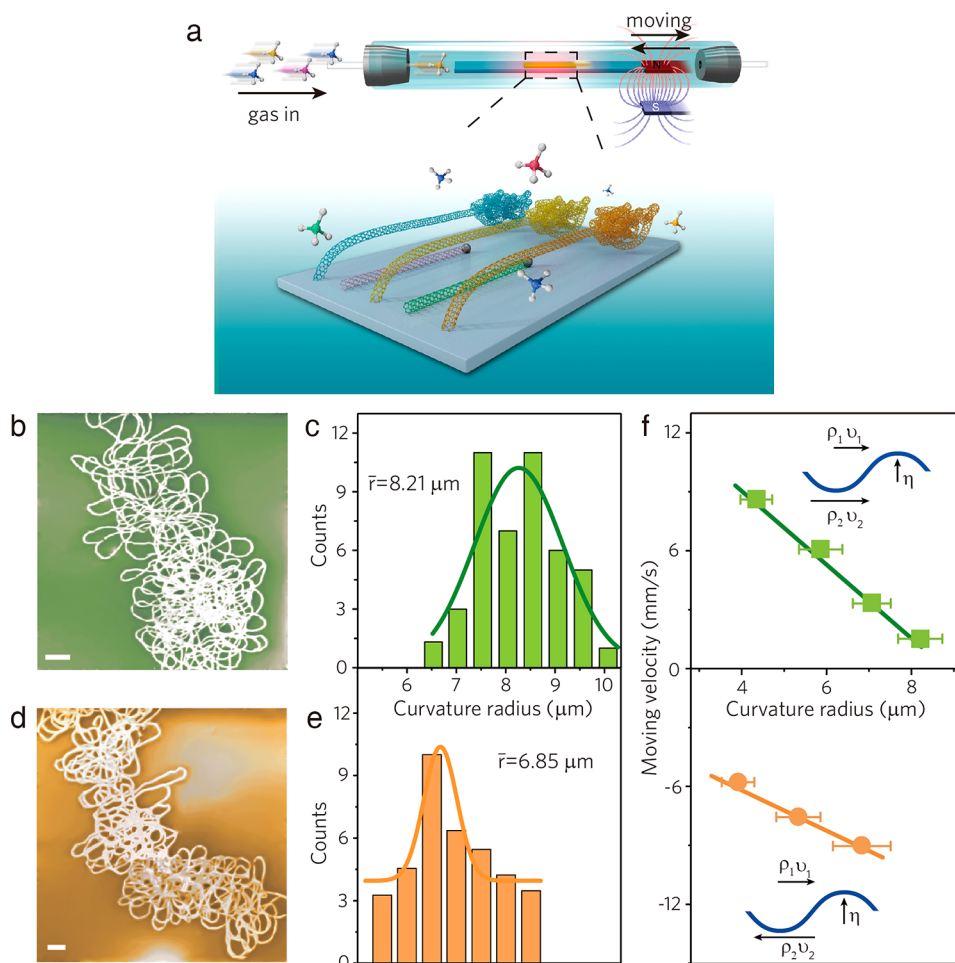


**Figure 1. Synthesis and scale control of CNT-Ts.** (a) Scheme for the synthesis of CNT-Ts. (b, d) Scanning electron microscope (SEM) images of CNT-Ts synthesized when the magnets move at  $v = 1.5 \text{ mm/s}$  in the same direction as the gas flow (b) and  $v = -9.1 \text{ mm/s}$  opposite to the direction of gas flow (d). Scale bars,  $15 \mu\text{m}$  in (b) and  $10 \mu\text{m}$  in (d). (c, e) Curvature radius distributions of secondary loops within CNT-Ts shown in (b) and (d), respectively. The solid lines are Gaussian fitting peaks. (f) Dependence of the average curvature radius on the moving velocity of the linkage system. Error bars represent the standard deviation of curvature radius in the as-grown CNT-Ts at definite conditions. The positive or negative moving velocity indicates that the linkage system moves along the same or opposite direction to the gas flow. The insets are schemes underlying the mechanism of KHI where  $\eta$  denotes the perturbation and  $\rho, v$  represent density, velocity of the two fluidic layers.

Aimed at target applications, it is feasible to manipulate the microstructures of these CNT materials for bottom-up molecular design. Despite unceasing demonstrations of agglomerated and vertically aligned CNTs,<sup>10</sup> there still lacks high-end applications of perfectly assembled ultralong CNTs, especially working as the precise device components. The stringent technical requirement has pointed out that the density of single-walled CNTs (SWNTs) should be higher than  $125 \mu\text{m}^{-1}$  (or the few walled CNTs higher than  $22 \mu\text{m}^{-1}$ ), while the metallic CNT (m-CNT) content must be lowered to the ppm level.<sup>14,15</sup> As predicted by the Schulz–Flory distribution,<sup>16</sup> the production of long tubes exponentially decreases with the CNT length. It can hardly achieve both the targets of high density and highly pure semiconducting CNTs (s-CNTs) at the same time. Therefore, it requires novel analysis or perspective of both the mechanism and strategies. If we regard the millions of ultralong CNTs produced in the same batch as a chaotic collection, the fractal rule will be the horizontal alignment of individuals at a definite spacing. Our recent attempts have demonstrated that rational organization of gas flow<sup>14,17,18</sup> is an appropriate route to flexibly reorganize

or alter the fractal rule, so as to achieve the multilevel assembly of the chaotic system. But it still lacks the precise analysis about the dependence of gas flow on the fractal geometry. It also remains ambiguous how the gas flow interacts with the floating nanotubes under the fluidic perturbation. Considering their flexibility, these ultralong CNTs can not only contribute to visualizing the hydrodynamic behaviors of flow but also acquire a better understanding for the rational synthesis and assembly of high aspect ratio low-dimensional nanomaterials.

## RESULTS AND DISCUSSION

Figure 1a schematically shows the synthesis of CNT-Ts. Ultralong CNTs grow continuously from the catalyst zone in the upstream of silicon substrates following the “kite-flying”<sup>11</sup> mechanism. Underneath the substrates, a long quartz boat is connected to a magnet placed in the low-temperature zone. Another magnet is located on the trail outside the reactor, of which the moving velocity can be precisely controlled by the electric motor. Under the effect of the as-formed magnetic field, it will attract the internal magnet to synchronously move back and forth at the same velocity. The ultralong CNTs were

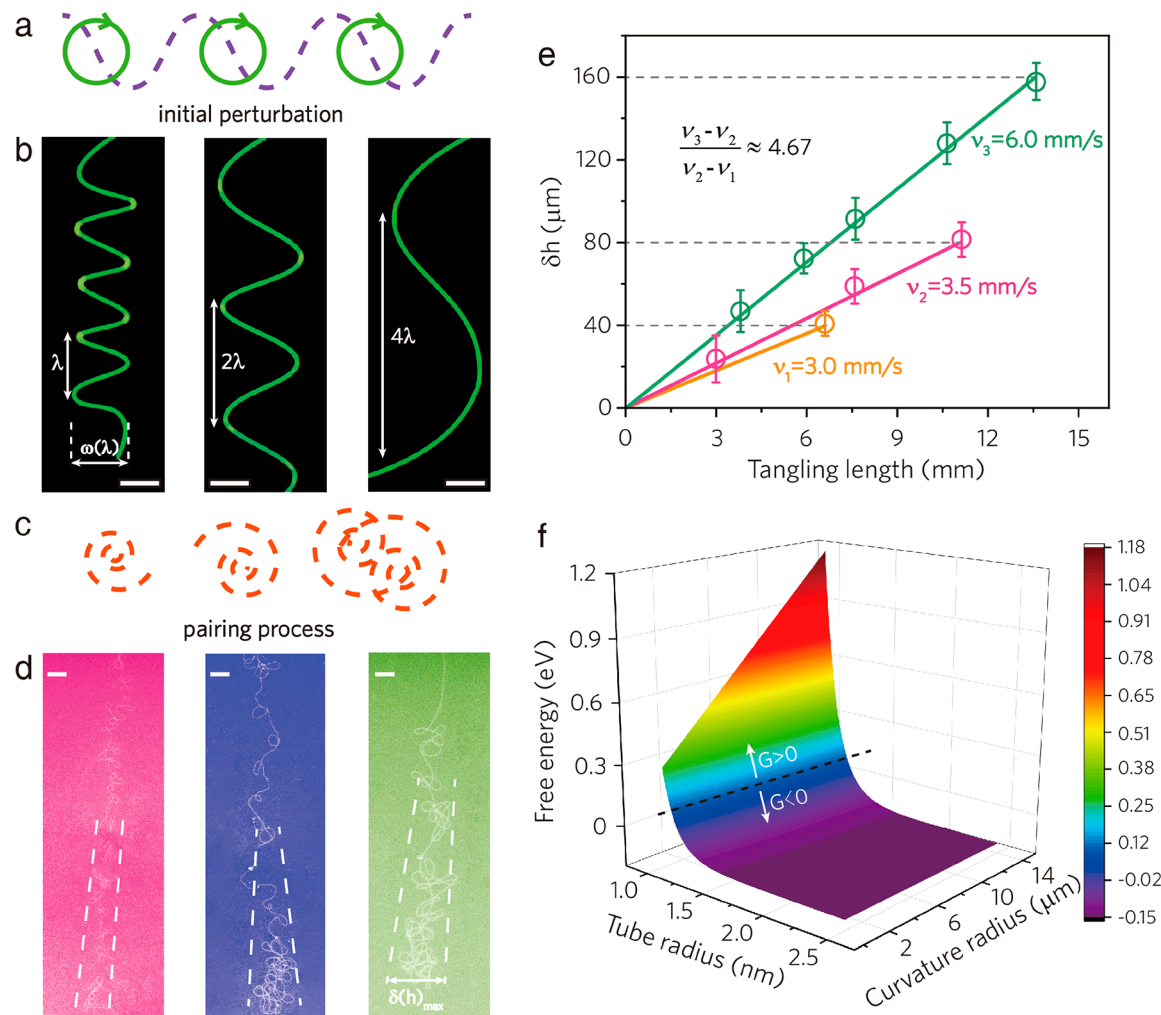


**Figure 2. Fractal geometry evolution and conformation energy of the CNT-Ts.** (a) Schematic setup of a vortex line representing a sinusoidal initial perturbation. Each circle represents a vortex formed between each maxima and its neighboring minima in the initial perturbation profile. (b) Resonant Rayleigh scattering (RRS) images of deformed ultralong CNTs grown under the same condition. The moving velocity of linkage system changes from  $-1.2$  to  $-2.2$  mm/s with a step of  $-0.5$  mm/s from left to right. Scale bars,  $10\text{ }\mu\text{m}$ . (c) Scheme for the pairing process of the CNT-T formation. The horizontal displacement  $\delta(h)_{\max}$  increases with the tangling length due to inverse cascade of vortices. (d) SEM images of the CNT-Ts grown under the same condition and moving velocity  $v = -6.5$  mm/s of linkage system. The white dotted lines signify the evolution of  $\delta(h)_{\max}$  with the tangling length. Scale bars,  $10\text{ }\mu\text{m}$ . (e) Dependence of  $\delta(h)$  on the tangling length under different moving velocities. The gray dotted lines indicate the horizontal displacement of terminal CNT-Ts. Errors come from the uncertainty when determining the boundary of as-formed CNT-Ts. Here, the tangling length denotes the length range where the CNT-T covers. It starts from the point when the straight CNT begins to curl. (f) Dependence of the free energy on the tube radius and curvature radius, which was modeled by Python 3.0.

first synthesized in laminar flow (the Reynold number  $\sim 10^{-2}$ ) with the routine process,<sup>16,19,20</sup> producing a dominant mixture of 17% SWNTs and 83% double-walled CNTs (DWNTs). The maximum length of DWNTs could be quickly up to decimeter scale, as the vapor-assisted kinetics triggered an ultrafast growth rate<sup>20</sup> around  $80\text{--}90\text{ }\mu\text{m/s}$  (Supporting Information Figure S1). Then the feedstock supply was terminated, and the magnets together with the quartz boat (defined as “linkage system”) were set to move at a minimal velocity for several seconds. It should be the micro perturbation that damaged the steady flow and led those floating ultralong CNTs to curled tangles. Because when there was no magnetic field, most of the as-grown CNTs were straight and horizontally aligned (Supporting Information Figure S1). It has been discovered that the moving direction and velocity of the linkage system determine the scale of CNT-Ts. When the linkage system moves along the same direction as the gas flow, the as-grown

CNT-Ts can be as large as  $0.1\text{ mm}^2$  (Figure 1b,c) with the average curvature radius approximately  $8.21\text{ }\mu\text{m}$ , whereas when they move along an opposite direction the CNT-T is smaller than  $0.07\text{ mm}^2$  (Figure 1d,e) and composed of loops with an average curvature radius around  $6.85\text{ }\mu\text{m}$ .

It can be seen from Figure 1f that the curvature radius of CNT-Ts is monotonically dependent on the moving velocity. Larger CNT-Ts are preferentially produced when the linkage system moves along the same direction as the flow. It is attributed to the different shear strength and relative velocities in fluidic layers. The laminar flow has become discontinuous above the substrate when the linkage system moves momentarily. It will lead to separated fluidic layers, near and away from the surface, with different hydrodynamic behaviors in which incompressible and inviscid fluids are in irrotational motion.<sup>21,22</sup> Flow field analysis has demonstrated the existence of vortices at the interface. If the linkage system moves along

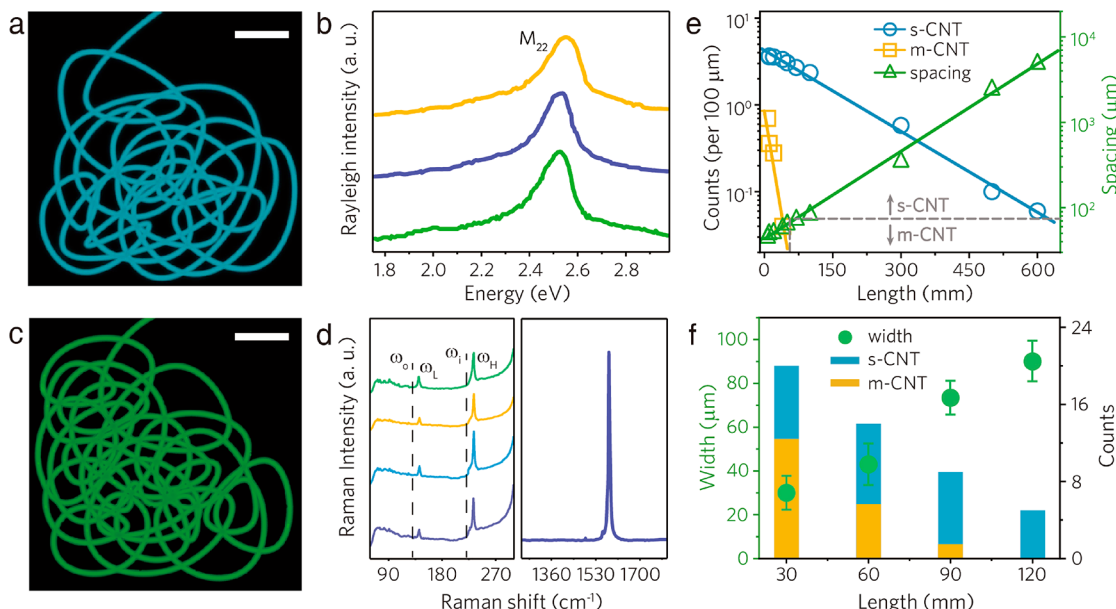


**Figure 3.** Spectroscopic characterization and statistics of metallic or semiconducting CNT-Ts. (a) Combined RRS image of a representative metallic CNT-T captured from different angles.<sup>14</sup> Scale bar, 15  $\mu\text{m}$ . (b) RRS spectra at different positions of the CNT-T in (a). The excitation photon energy of 2.33 eV is in resonance with  $M_{22}$  electronic transition. (c) RRS image of a representative semiconducting CNT-T. Scale bar, 15  $\mu\text{m}$ . (d) Raman spectra for the CNT-T shown in (c) weaved from a DWNT. A representative G band for the CNT-T with Lorentz line shape is shown on the right side. (e) Quantity statistics of m- and s-CNTs at the same length. A length dependence of the intertube spacing has been shown to the right coordinate. The gray dotted lines indicate the critical status which facilitates easy separation of s- and m-CNTs. (f) Dependence of CNT quantity on the length. The blue and yellow portions of the column charts indicate the quantity of s- and m-CNTs, respectively. Data of average width for the as-formed CNT-Ts are shown to the left coordinate. Error bars represent the standard deviation of five CNT-Ts grown at different length.

the same direction as the flow, vortices appear away from the substrate with a wider coverage (Supporting Information Figure S2). It is because the flow will move backward at a larger velocity relative to the linkage system (Text S1). In comparison, narrower vortices have been witnessed close to the surface of substrate while moving along the opposite direction (Supporting Information Figures S3 and S4). The CNTs will be under tension due to the positive relative velocity. Those as-formed vortices can thus be stretched into narrower ones, leading to smaller CNT-Ts. Despite that, the interface between fluidic layers on both occasions acts as an unstable vortex sheet that rolls up into a spiral under the perturbation, which actually addresses the process of KHI in classical hydrodynamics.<sup>21,23</sup> In each fluidic layer, the velocity and density profiles are uniform but discontinuous at the interface. It can be regarded as flows with a tangential velocity difference, at which small perturbations along the interface evolve into a number of large vortices. The floating ultralong CNTs are flexible enough to be aligned with the flow pattern.

However, further experiments have demonstrated that these individual ultralong CNTs might form other fractals instead of tangles at lower moving velocity (<1 mm/s). Because weaker perturbation contributes to an array of single-mode point vortices<sup>22</sup> aligned along the discontinuity surface (Figure 2a). It will lead to a sinuous and symmetric geometry (Figure 2b), as the vortices are kept in place due to the zero net velocities.<sup>21</sup> The distance between neighboring peaks  $\lambda$  multiplies when the moving velocity of linkage system increases at equal steps (Text S2). The horizontal displacement  $\omega(\lambda)$  will exponentially increase with the moving velocity. It has implied the trend toward weakened central potential of vortices, leading to

continuously broadened sinuous CNTs (Supporting Information Figure S5).

As the moving velocity continues to increase, the fluidic layers begin to mix under stronger perturbation. It has caused nonlinear paired vortices<sup>24</sup> increasing in size and decreasing in number (Figure 2c), which finally leads to CNT-Ts with chaotic aperiodicity. However, it is indeed an advanced orderly pattern which is affected by the bounded periodicity. All the as-formed tangles are limited within a definite horizontal displacement  $\delta(h)_{\max}$  (Figure 2d), showing an obvious linear dependence on the tangling length regardless of moving velocities (Figure 2e). Slopes of length dependence profiles are proportional to the moving velocity. It can be described by

$$\delta(h)_{\max} \cong 0.2\Delta\nu L/U \quad (1)$$

where  $\Delta\nu$ ,  $L$ , and  $U$  denote the moving velocity, tangling length, and gas velocity, respectively. A statistic of 30 samples indicates that the  $\delta(h)_{\max}$  can be periodically multiplied (Figure 2e) as long as the neighboring moving velocities increase at a constant ratio of 4.67. It equals to the Feigenbaum number which originally expresses the ratio of limits between consecutive bifurcation diagrams of a nonlinear assembly.<sup>25</sup> Such a bifurcation at a definite rate acts as the fractal rule to direct the macroscopic structure of CNT-Ts, revealing a paradigm for the evolution of horizontal displacement. In addition, according to the calculations of free energy shown in Figure 2f, we have discovered that spontaneous formation of CNT-Ts only dominates in the area of larger tube radius and curvature radius. It indicates that the larger vortices are thermodynamically more stable due to the higher moment of inertia, which contributes to the loop formation with a larger curvature radius. Those CNTs with larger radius or multiple

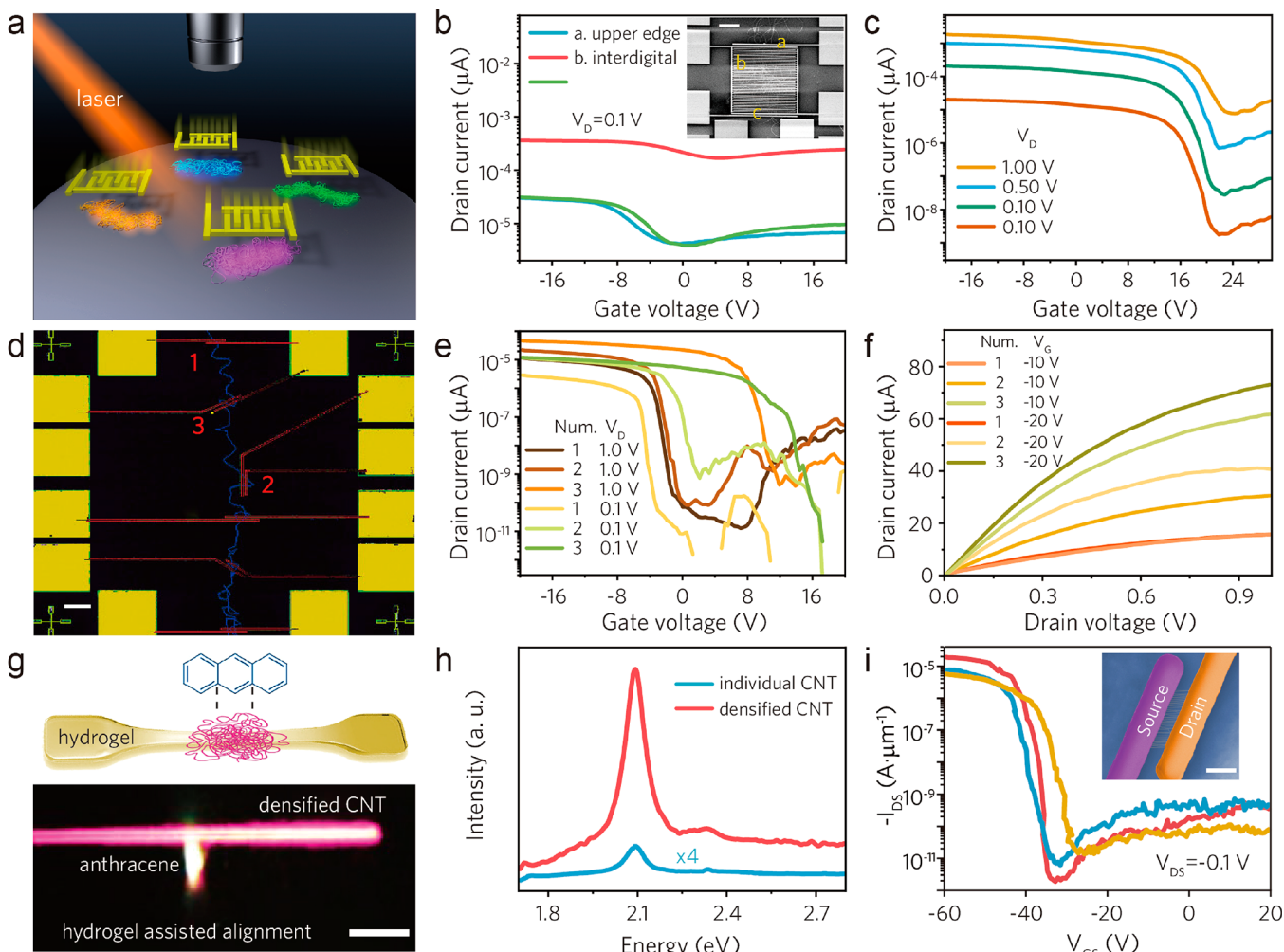


**Figure 4. Electrical properties of CNT-Ts.** (a) Scheme for the direct FET fabrication after a spectroscopic separation. (b) Transfer characteristics of the transistor fabricated on a metallic CNT-T. Inset, SEM image of the same back-gated transistor with a channel length of 700 nm. Scale bar, 50  $\mu\text{m}$ . (c) Transfer characteristics of the transistor fabricated on a semiconducting CNT-T. (d) SEM image of transistors fabricated on a sinuous CNT. The numbers in red indicate the quantity of CNTs contacted by electrodes. Scale bar, 50  $\mu\text{m}$ . (e) Transfer characteristics of the different devices shown in (d). (f) Output characteristics of the same devices shown in (d). (g) The upper panel is the scheme for the strategy of hydrogel assisted alignment on CNT-Ts. The gray dotted line indicates the interaction between anthracene and CNT-T. The below is one representative RRS image of the aligned CNT-T. Scale bar, 10  $\mu\text{m}$ . (h) RRS spectra of the aligned CNT-T. The intensity of individual CNT has been four times multiplied so as to be clearly exhibited. (i) Transfer characteristics of three FETs fabricated on the aligned CNT-Ts. The inset is a SEM image of an FET device fabricated with a representative aligned CNT-T as the channel material and a channel length of 4  $\mu\text{m}$ . Scale bar, 10  $\mu\text{m}$ .

walls possess a higher rigidity, which makes them hard to bend to a large angle.

It has noted that a CNT-T is composed of a large number of basic units attracted and self-organized under definite fractal rules. The secondary loops are able to adjust their behaviors based on interaction with surrounding circumstances, so as to form a matter tolerant of variable environment. Energy consumption will be required during the evolution of CNT-Ts, which is the basis of the entropy increase and lowest dissipation indicated by the Feigenbaum number model. It is the fractal rule that makes the horizontal displacement preferentially evolve according to the principle of periodic multiplication, so that those individual ultralong CNTs are able to be curled under minimum resistance. In addition, such fractal rules can be precisely altered by changing the moving velocity so as to manipulate their microscopic curvature radius. Therefore, the foundation and close association of geometry control based on fractal and chaos have been formed.

Additionally, the length of the ultralong CNT from which the CNT-T is formed will play an important role in its selective synthesis. As indicated in our recent report about rate-selected CNT growth,<sup>13</sup> spontaneous purification of the predicted 99.9999% s-CNTs has been witnessed based on the interlocking mechanism. It has revealed that shorter CNTs are predominantly m-CNTs with a narrower diameter while the longer ones are statistically double-walled and semiconducting species. Combined with the curvature intensified spectroscopy, it would be effective to separate semiconducting CNT-Ts from their metallic counterparts *via* the RRS characterization. One thing that should be emphasized is that the m-CNTs mentioned here are either SWNTs or DWNTs containing any metallic components, while the s-CNTs refer to ones with all-semiconducting layers.

RRS images of a metallic and semiconducting CNT-T grown in a same batch are shown in Figure 3a,c. Uniform height profiles in the atomic force microscope (AFM) have

demonstrated their consistent structures (*Supporting Information Figure S6*). Micro-Raman measurements on the CNT-T at random positions in *Figure 3a* show radial breathing mode (RBM) peaks concentrated at  $\sim 116\text{ cm}^{-1}$  (*Supporting Information Figure S7*), despite minimal offsets resulting from external circumstances. The corresponding G mode at  $\sim 1580\text{ cm}^{-1}$  exhibits a typical Breit–Wigner–Fano (BWF) line shape featuring metallic CNTs. The chirality of (16, 13) was assigned by comparison with the Kataura plot<sup>26</sup> SWNTs. This assignment was further verified by the Rayleigh spectra on the same CNT-T, which all show a concentration at  $\sim 2.55\text{ eV}$  (*Figure 3b*), consistent with the optical transition atlas.<sup>27</sup> Another green CNT-T (*Figure 3c*) possesses a typical feature of s-CNTs with the measured micro-Raman G mode exhibiting a Lorentz line shape (*Figure 3d*). A transmission electron microscope (TEM) image and electron diffraction measurement (*Supporting Information Figure S7*) indicate the CNT-T is weaved from a DWNT of the chirality (8, 7)@(17, 8). RBM modes measured from random positions of the green CNT-T are concentrated at  $\sim 143\text{ cm}^{-1}$  for in-phase ( $\omega_L$ ) and  $\sim 235\text{ cm}^{-1}$  for out-of-phase ( $\omega_H$ ) (*Figure 3d*), appearing almost dozens of frequencies' blue-shift<sup>28</sup> from those for constituent outer- ( $\omega_o$ ) and inner-wall SWNTs ( $\omega_i$ ). Meanwhile, nonsharp disorder-induced D bands around  $\sim 1350\text{ cm}^{-1}$  in Raman measurements of both CNT-Ts indicate that the synthesized CNT-Ts are of high quality.<sup>29</sup> Monowavelength lasers (2.33 eV, 1.96 eV, 1.58 eV) that we utilized have covered most of the common tube families including the major distribution of the as-grown m-CNTs. Due to the quantum coupling, resonance of at least one layer with the laser determines the excitation of both concentric layers for a DWNT. Therefore, it can promise the robustness in identifying the metallic components *via* the spectroscopic characterizations. The statistics of the RBMs for multibatch samples give an estimate of  $\sim 100\%$  semiconducting CNT-Ts without the BWF signature. Some particular chiral indices indicating larger chiral angles appear more frequently in SWNTs or concentric layers of DWNTs (*Supporting Information Figure S8*).

Furthermore, in order to precisely obtain metallic or semiconducting CNT-Ts, it is a prerequisite to probe the length dependence profiles for the intertube spacing and content of CNTs with definite conductive properties. Careful micro-Raman measurements were performed on free-standing ultralong CNTs to count the m- and s-CNTs at different length.<sup>13</sup> It has been demonstrated that the decay rate of m-CNTs is nearly 10 times faster than that of s-CNTs (*Figure 3e*). The m-CNT content will drop to 0.7% at the length of 50 mm where the intertube spacing is  $\sim 70\text{ }\mu\text{m}$  (*Figure 3e*). It is a critical status to separate almost pure semiconducting CNT-Ts without any metallic impurity or overlapping with neighboring CNTs. “Cleaner” semiconducting CNT-Ts can be easier to obtain at length  $>50\text{ mm}$ , but it will be difficult to separate metallic CNT-Ts in the shorter-length area because of the higher density. Despite that, it has shown an opposite trend for the length dependence between the width of CNT-Ts and m-CNT content (*Figure 3f*). The average width is much smaller for both metallic and semiconducting CNT-Ts in the short-length areas ( $<30\text{ mm}$ ), and the m-CNTs are highly enriched. This means that the metallic CNT-Ts are generally narrower and sparsely aligned as they are formed from shorter CNTs. Based on such a balance, 85% metallic CNT-Ts were successfully enriched at the corresponding length position  $\sim 20\text{ mm}$  (*Supporting Information Figure S9*).

As these CNT-Ts, either metallic or semiconducting, can be directly synthesized and separated on the Si/SiO<sub>2</sub> substrate, they have contributed significantly to facile device fabrication and electrical measurements (*Figure 4a*). The inset of *Figure 4b* shows the SEM image of a typical field-effect transistor (FET) from a metallic CNT-T with the channel length of 700 nm. An individual long CNT was tangled within the region b, leaving the initial and terminal part at a and c region, respectively. As shown in *Figure 4b*, the device delivered a current of  $380\text{ }\mu\text{A}$  with on/off ratio around 3. The output currents of the upper- and lower-edge regions are much lower than that of tangle. But their electrical characteristics are almost the same, which indicates the chiral-consistency of the whole CNT-T. Following the simple RRS identification, another device was fabricated on a semiconducting CNT-T. It has delivered a current of  $2\text{ mA}$  at  $V_D = 1\text{ V}$  with an on/off ratio close to  $10^5$  (*Figure 4c*).

Therefore, aimed at the excellent carbon-based electrical applications, these CNT-Ts contribute significantly to separating and manipulating high-aspect-ratio ultralong CNTs, leading to considerable current output. It has demonstrated a feasible route for compatibility between high structural selectivity and high areal density for ultralong CNTs. However, we have noticed that the on/off ratio is still not as high as that of individual s-CNTs we previously reported<sup>14</sup> ( $10^7$ – $10^8$ ). Therefore, in order to explore the influence of such curved structures, we have fabricated a device based on the long curved CNT (*Figure 4d*). Electrodes were contacted on CNT portions which all came from one sinuous ultralong CNT. Parts e and f of *Figure 4* present their transfer and output characteristics, respectively. The output current increased proportionally with the quantity of contacted CNTs (*Text S3*). But the on/off ratio dropped by orders of magnitude when the contacted CNTs increased from one to three. We assume that it is the strain from the curved structure that results in anomaly of electrical characteristics. When the CNTs are curled, it will cause extra resistance to broaden the bandgap so as to decrease the conductivity of CNTs.<sup>30</sup> At the off state, the conduction and valence bands will be synchronously adjusted because electrons and holes are equally affected. On the on-state, despite similar resistance induced by strain, the inner walls of DWNTs will also contribute to the output delivery. The conduction band cannot be uplifted as high as that of SWNTs, which has led to lower on/off ratio of DWNTs.

To verify our assumptions, an *ex situ* strategy was developed to alter the fractal of CNT-Ts into the aligned morphology with liquefied anthracene, that is, the hydrogel-assisted alignment. The scheme has been shown in the upper panel of *Figure 4g* and below is one representative RRS image of the aligned CNT-T. Although a little anthracene still remains, the treatments have not caused obvious damage to the CNT-Ts (*Supporting Information Figure S10*). In addition, the spectroscopic intensity is  $\sim 20$  times higher than that of individual CNTs, revealing that the density has been increased to  $\sim 20\text{ CNTs }\mu\text{m}^{-1}$ . Furthermore, back-gated FETs were fabricated on different aligned CNT-Ts as shown in the inset of *Figure 4i*. The transfer characteristics of three devices in *Figure 4i* show increased on/off ratio around  $10^6$ – $10^7$ , which can best demonstrate our hypothesis. The nonuniform electrical characteristics are possibly due to the CNTs with different diameters and bipolar behaviors,<sup>31,32</sup> which was proved further by the Raman and AFM characterization

(Supporting Information Figure S11). Despite that, it is approaching the ultimate target of dense few walled CNTs with consistent chirality<sup>14</sup> ( $\sim 22$  CNTs  $\mu\text{m}^{-1}$ ). It is a paradigm for the application of these flexible ultralong CNTs by switching their fractal geometry, which can increase the surface current without altering their chiral structures.

## CONCLUSION

In summary, we have proposed a technical route to obtain highly pure metallic, semiconducting, or chirality-specific CNT aggregates without introducing any structural defects. By *in situ* manipulating the fractal geometry, chaotic CNT-Ts can be selectively enriched with variable curvature radius in an entropy-driven process of instability. In addition, with the assistance of intensified spectroscopy, these CNT-Ts can be easily identified and separated. It has markedly simplified the device fabrication process and contributed significantly to the applications of high-output devices. The route of “simultaneous synthesis and separation” is an effective practice in utilizing the chaos by switching fractals of horizontally aligned ultralong CNTs. It will be robust to connect the synthesis, separation and fabrication processes in the field of low dimensional nano electronics, which will stimulate emerging functional device applications in aerospace, electronics, biosensors, robots, mechanics, etc.

## METHODS

**Synthesis of CNT-Ts by Magnetron Weaving.**  $\text{FeCl}_3$  ethanol solution (0.03 mol·L<sup>-1</sup>) was deposited as a catalyst precursor onto silicon substrates with an 800 nm thick  $\text{SiO}_2$  coating layer. The temperature was increased at a rate of 30–35 °C min<sup>-1</sup> at an atmosphere of  $\text{H}_2/\text{Ar}$  and kept 1005 °C for 15 min. Then  $\text{CH}_4$  and  $\text{H}_2$  ( $V_{\text{H}_2}/V_{\text{CH}_4} = 2:1$ ;  $F_{\text{total}} = 75$  sccm, with 0.5%  $\text{H}_2\text{O}$ ) were inlet into the reactor continuously for a duration of 30 min. Approaching the end of reaction, the external magnet was electrically started to move along the same as or opposite to the direction of the gas flow. Then the gas mixture was switched to the original composition,  $V_{\text{H}_2}/V_{\text{Ar}} = 2:1$ ;  $F_{\text{total}} = 150$  sccm, until it was cooled to room temperature.

**Resonant Raman Spectra and Mapping.** Raman spectra were acquired with Horiba HR 800 equipped with a liquid-nitrogen-cooled silicon CCD detector.<sup>13</sup> Three laser excitation sources were used, including 532 nm (2.33 eV), 633 nm (1.96 eV), and 785 nm (1.58 eV). The scattered light was collected through a 100× air objective using a backscattering configuration (the laser spot size is  $\sim 1 \mu\text{m}^2$ ). Stokes Raman spectra were acquired with edge filters cutting at 100 cm<sup>-1</sup>. A 600 grooves per millimeter grating rate was used, giving a spectral resolution better than 2 cm<sup>-1</sup>. The laser power was kept at or below  $\sim 1$  mW to avoid the heating effect. For the quantity statistics of m- and s-CNTs at different CNT lengths, the substrates are silicon wafers with 300 nm thick thermal oxide on the surface, containing slits (300 nm deep, 5–20  $\mu\text{m}$  wide) and marks fabricated by photolithography and dry etching. The measurement was conducted within a stage, preceded an annealing process carried out at 450 °C for 15 min under 100 sccm Ar flow. Raman spectra were collected at the center of 1500 cm<sup>-1</sup> (covering 1200–1700 cm<sup>-1</sup>) for D and G modes. Then, in order to construct an image, Raman spectra were acquired by raster scanning a wide area including the specific CNT-T with a 0.2 mm step size. Typical accumulation time was 60 s for each spectrum. For each CNT Raman peak, G<sup>+</sup>, G<sup>-</sup> and D, two spectral windows were chosen, one for the signal itself and one to remove featureless background contributions.

**Other Characterizations of CNT-Ts.** The as-grown samples were inspected with SEM (JSM 7401F, 1.0 kV), TEM (JEM 2010, 120.0 kV), and AFM (Asylum Cypher) to characterize the morphology or identify the atomic structure. An optical microscope (long working

distance metallography microscope, FS 70Z) and supercontinuum laser was utilized for resonant Rayleigh scattering.

**Conformation Energy and Entropy of CNT-Ts.** The total free energy for the formation of CNT-Ts can be expressed as

$$G = E_c + E_v - TS \quad (2)$$

where  $T$  and  $S$  denote the growth temperature and configurational entropy, respectively.  $E_v$  is the van der Waals energy<sup>33</sup> addressing the mutual interaction of secondary loops, and  $E_c$  is the curvature elastic energy of graphite layers<sup>34</sup> that has revealed the potential in curling CNTs. From the definition of entropy, one has the conformation energy of CNT-Ts

$$S = k_B \ln \Omega = k_B f(R, r) \quad (3)$$

where  $k_B$  denotes the Boltzmann constant and  $f(R, r)$  addresses the function of curvature radius  $R$  and tube radius  $r$ . It should be noted that the mixing entropy derived from pentagon-heptagon defects<sup>35</sup> has been neglected because these CNT-Ts are perfectly assembled in hexagonal network. The entropy of CNT-Ts depends on the total number of carbon atoms without consideration of the pentagon-heptagon atomic defects. It can be expressed as shown

$$S = k_B \ln \Omega = k_B \ln \left( 4\pi^2 \frac{Rr}{a^2} + \frac{\sqrt{3}}{\sqrt{2}} \pi \frac{\sqrt{Rr}}{a} - 6 \right) \quad (4)$$

where  $k_B$  denotes the Boltzmann constant,  $R$  denotes the curvature radius of CNT-Ts,  $r$  is the tube radius, and  $a$  is the distance between adjacent carbon atoms, 1.421 Å. The curvature elastic energy of a single layer curved graphite CNT has been proposed in terms of a two-dimensional lattice.<sup>36,37</sup> It can be expressed with the function

$$E_c = \frac{2\pi^2 k_c R}{r\sqrt{1 - (r/R)^2}} \quad (5)$$

where  $k_c$  is estimated to be 1.2 eV from the measured phonon spectrum of graphite. In addition, the van der Waals intertube adhesion energy is a long-range dispersion interaction of carbon pairs described by the Lennard-Jones potential,<sup>38</sup>  $u = -A/d^6 + B/d^{12}$ , where  $d$  is the carbon–carbon distance,  $A = 15.16$  eV Å<sup>6</sup>, and  $B = 2.4 \times 10^4$  eV Å<sup>12</sup> are characteristic of the attractive and repulsive interactions of the graphite. Then the total van der Waals interaction energy is

$$E_v = \frac{9\pi^2 n_\sigma^2 R}{2r^3} \left( -AI_A + \frac{21B}{32r^6} I_B \right) \quad (6)$$

where  $n_\sigma = 4/(3\sqrt{3}a^2)$  denotes the carbon atom density.  $I_A$  and  $I_B$  are constants describing the relative positions between neighboring tubes.

**Fabrication and characterization of devices.** Titanium/palladium (Ti/Pd 0.5/70 nm) electrodes were patterned on Si/SiO<sub>2</sub> substrates with an 800 nm SiO<sub>2</sub> top layer using electron beam lithography and electron beam evaporation. This was preceded by formation of titanium/gold (Ti/Au 5/40 nm) probe pads with similar fabrication process as Ti/Pd contacts. Electronic characterizations were carried out with a Keithley 2612B sourcemeter at room temperature in air.

**Transfer Procedure of CNT-Ts from the Growth Substrate to the PTFE.** About 10  $\mu\text{L}$  of acetone liquid was dropped onto the growth substrate, so that the substrate and specific CNT-Ts were immersed by acetone.<sup>19</sup> A cellulose acetone film was utilized to cover the substrate quickly and pressed tightly on the substrate. With the vaporization of acetone, the film was carefully peeled off from the substrate, and ideally, the specific CNT-Ts were attached onto the peeled film. Then,  $\sim 10 \mu\text{L}$  acetone solution was dropped onto the PTFE to make it wet, allowing the close contact of PTFE with the film. PTFE with film on it was soaked in 100 mL of acetone for 30 min to wash out the cellulose acetone. Finally, the PTFE was taken out and placed horizontally on a clean glass substrate. It is better to spout 50 mL of acetone onto the PTFE to ensure total dissolution of the residuals of cellulose acetone.

**Synthesis of Hydrogels.** The procedure for the synthesis of poly(vinyl alcohol) (PVA) hydrogel refers to that developed by Zhao's group.<sup>39</sup> It was synthesized from 10 wt % PVA (99%-hydrolyzed, Sigma-Aldrich, 363065) solution. First, the solution was heated in the water bath at 100 °C with stirring for 5 h. After the treatment of mixing and defoaming, the 10 wt % PVA solutions were poured into a mold and frozen at -20 °C for 10 h followed by thawing at room temperature for 2 h. Further, the hydrogel was dried in an incubator at 40 °C for 1 h and then annealed at 100 °C for 20 min. The as-synthesized hydrogel was kept in water to maintain an equilibrium state.

**Hydrogel-Assisted Alignment of CNT-Ts.** An optically identified CNT-T was transferred onto the PTFE under the assistance of cellulose acetate film.<sup>19</sup> Then the sample was placed into the argon-filled glovebox for subsequent treatments, so as to keep the CNT-Ts from oxygen. The liquefied anthracene (~10 μL) was dropped onto the CNT-T followed by heating at 200 °C for 30 min. The anthracene was gradually shrunk into a small droplet on the heated surface. Subsequently, the as-synthesized hydrogel was stuck to the CNT-T on the PTFE, so that the CNT-T could be aligned into a horizontal array as the hydrogel was continuously stretched. Finally, the residual hydrogel and anthracene on the surface of CNT-Ts were removed by heating at 300 °C for 1 h.

## ASSOCIATED CONTENT

### Supporting Information

The Supporting Information is available free of charge at <https://pubs.acs.org/doi/10.1021/acsnano.0c10300>.

Description of the trend of curvature radius changing with the moving velocity, Kelvin–Helmholtz instability, and difficulties in measuring the saturated current; figures showing the synthesis of CNT-Ts and ultralong CNTs, modeling of the flow field with the movement of linkage system, morphology analysis of the CNT-Ts, characterization and statistics of CNT-Ts, and evaluation of the device performances ([PDF](#))

## AUTHOR INFORMATION

### Corresponding Author

**Fei Wei** – Beijing Key Laboratory of Green Chemical Reaction Engineering and Technology, Department of Chemical Engineering, Tsinghua University, Beijing 100084, China; [orcid.org/0000-0002-1422-9784](https://orcid.org/0000-0002-1422-9784); Email: [wf-dce@mail.tsinghua.edu.cn](mailto:wf-dce@tsinghua.edu.cn)

### Authors

**Zhenxing Zhu** – Beijing Key Laboratory of Green Chemical Reaction Engineering and Technology, Department of Chemical Engineering, Tsinghua University, Beijing 100084, China; [orcid.org/0000-0001-8060-0775](https://orcid.org/0000-0001-8060-0775)

**Nan Wei** – Key Laboratory for the Physics and Chemistry of Nanodevices, Peking University, Beijing 100871, China

**Bowen Yan** – School of Aerospace Engineering, Tsinghua University, Beijing 100084, China

**Boyuan Shen** – Beijing Key Laboratory of Green Chemical Reaction Engineering and Technology, Department of Chemical Engineering, Tsinghua University, Beijing 100084, China

**Jun Gao** – Beijing Key Laboratory of Green Chemical Reaction Engineering and Technology, Department of Chemical Engineering, Tsinghua University, Beijing 100084, China; [orcid.org/0000-0002-3847-0839](https://orcid.org/0000-0002-3847-0839)

**Silei Sun** – Beijing Key Laboratory of Green Chemical Reaction Engineering and Technology, Department of

Chemical Engineering, Tsinghua University, Beijing 100084, China

**Huanhuan Xie** – Beijing Key Laboratory of Green Chemical Reaction Engineering and Technology, Department of Chemical Engineering, Tsinghua University, Beijing 100084, China

**Hao Xiong** – Beijing Key Laboratory of Green Chemical Reaction Engineering and Technology, Department of Chemical Engineering, Tsinghua University, Beijing 100084, China

**Chenxi Zhang** – Beijing Key Laboratory of Green Chemical Reaction Engineering and Technology, Department of Chemical Engineering, Tsinghua University, Beijing 100084, China; [orcid.org/0000-0002-5736-9285](https://orcid.org/0000-0002-5736-9285)

**Rufan Zhang** – Beijing Key Laboratory of Green Chemical Reaction Engineering and Technology, Department of Chemical Engineering, Tsinghua University, Beijing 100084, China; [orcid.org/0000-0003-1774-0550](https://orcid.org/0000-0003-1774-0550)

**Weizhong Qian** – Beijing Key Laboratory of Green Chemical Reaction Engineering and Technology, Department of Chemical Engineering, Tsinghua University, Beijing 100084, China; [orcid.org/0000-0002-1684-1061](https://orcid.org/0000-0002-1684-1061)

**Song Fu** – School of Aerospace Engineering, Tsinghua University, Beijing 100084, China

**Lianmao Peng** – Key Laboratory for the Physics and Chemistry of Nanodevices, Peking University, Beijing 100871, China; [orcid.org/0000-0003-0754-074X](https://orcid.org/0000-0003-0754-074X)

Complete contact information is available at:

<https://pubs.acs.org/10.1021/acsnano.0c10300>

### Author Contributions

<sup>II</sup>Z.Z. and N.W. contributed equally to this work.

### Author Contributions

F.W., Z.Z., L.P., and N.W. conceived and designed the experiments. Z.Z., N.W., B.S., H.X., S.S., H.X., and J.G. performed the experiments. H.X. and S.S. were responsible for the technical assistance with the electron diffraction pattern of carbon nanotubes using HRTEM. Z.Z., N.W., B.S., S.S., B.Y., C.Z., and J.G. performed the data analysis. Z.Z., W.Q., S.F., and R.Z. wrote the manuscript. All authors discussed the results and commented on the manuscript.

### Notes

The authors declare no competing financial interest.

## ACKNOWLEDGMENTS

We are grateful to D. Zhang (Peking University, China), Y. Hu (Tsinghua University, China), and L. Wang (Tsinghua University, China) for discussions. This work was supported by the Ministry of Science and Technology of China (2016YFA0200101, 2016YFA0200102, 2018YFB0604801, 2020YFC2201100, and 2020YFA0210700), the National Natural Science Foundation of China (21636005, 22075163, S1872156, 21908125, 61321001, 61427901-002, 61390504, and 61271051), Beijing Municipal Science and Technology Commission (Z151100003315009), and Science Challenge Project (TZ2016001).

## REFERENCES

- (1) Andrievskii, B. R.; Fradkov, A. L. Control of Chaos: Methods and Applications. II. Applications. *Autom. Remote Control* **2004**, 65, 505–533.

- (2) Fleck, R. The ‘Radcliffe Wave’ as a Kelvin–Helmholtz Instability. *Nature* **2020**, *583*, E24–E25.
- (3) Goldberger, A. L.; Rigney, D. R.; West, B. J. Science in Pictures: Chaos and Fractals in Human Physiology. *Sci. Am.* **1990**, *262*, 42–49.
- (4) Mandelbrot, B. B. *The Fractal Geometry of Nature*, 1st ed.; Macmillan: London, 1983.
- (5) Yang, T.; Zhao, Y. L.; Li, W. P.; Yu, C. Y.; Luan, J. H.; Lin, D. Y.; Fan, L.; Jiao, Z. B.; Liu, W. H.; Liu, X. J.; Kai, J. J.; Huang, J. C.; Liu, C. T. Ultrahigh-Strength and Ductile Superlattice Alloys with Nanoscale Disordered Interfaces. *Science* **2020**, *369*, 427.
- (6) Wang, D.; Fernandez-Martinez, A. Order from Disorder. *Science* **2012**, *337*, 812.
- (7) Egolf, D. A.; Greenside, H. S. Relation Between Fractal Dimension and Spatial Correlation Length for Extensive Chaos. *Nature* **1994**, *369*, 129–131.
- (8) Service, R. F. Chipmakers Look Past Moore’s Law, and Silicon. *Science* **2018**, *361*, 321.
- (9) Avouris, P.; Chen, Z.; Perebeinos, V. Carbon-based Electronics. *Nat. Nanotechnol.* **2007**, *2*, 605.
- (10) Zhang, Q.; Huang, J.-Q.; Qian, W.-Z.; Zhang, Y.-Y.; Wei, F. The Road for Nanomaterials Industry: A Review of Carbon Nanotube Production, Post-Treatment, and Bulk Applications for Composites and Energy Storage. *Small* **2013**, *9*, 1237–1265.
- (11) Huang, S.; Woodson, M.; Smalley, R.; Liu, J. Growth Mechanism of Oriented Long Single Walled Carbon Nanotubes Using “Fast-Heating” Chemical Vapor Deposition Process. *Nano Lett.* **2004**, *4*, 1025–1028.
- (12) Zhang, R.; Zhang, Y.; Wei, F. Controlled Synthesis of Ultralong Carbon Nanotubes with Perfect Structures and Extraordinary Properties. *Acc. Chem. Res.* **2017**, *50*, 179–189.
- (13) Zhu, Z.; Wei, N.; Cheng, W.; Shen, B.; Sun, S.; Gao, J.; Wen, Q.; Zhang, R.; Xu, J.; Wang, Y.; Wei, F. Rate-Selected Growth of Ultrapure Semiconducting Carbon Nanotube Arrays. *Nat. Commun.* **2019**, *10*, 4467.
- (14) Zhu, Z.; Wei, N.; Xie, H.; Zhang, R.; Bai, Y.; Wang, Q.; Zhang, C.; Wang, S.; Peng, L.; Dai, L.; Wei, F. Acoustic-Assisted Assembly of an Individual Monochromatic Ultralong Carbon Nanotube for High On-Current Transistors. *Sci. Adv.* **2016**, *2*, No. e1601572.
- (15) Franklin, A. D. The Road to Carbon Nanotube Transistors. *Nature* **2013**, *498*, 443.
- (16) Zhang, R.; Zhang, Y.; Zhang, Q.; Xie, H.; Qian, W.; Wei, F. Growth of Half-Meter Long Carbon Nanotubes Based on Schulz–Flory Distribution. *ACS Nano* **2013**, *7*, 6156–6161.
- (17) Zhu, Z.; Bai, Y.; Wei, N.; Gao, J.; Sun, S.; Zhang, C.; Wei, F. Controlled Growth of Crossed Ultralong Carbon Nanotubes by Gas Flow. *Nano Res.* **2020**, *13*, 1988–1995.
- (18) Bai, Y.; Zhang, R.; Ye, X.; Zhu, Z.; Xie, H.; Shen, B.; Cai, D.; Liu, B.; Zhang, C.; Jia, Z.; Zhang, S.; Li, X.; Wei, F. Carbon Nanotube Bundles with Tensile Strength over 80 GPa. *Nat. Nanotechnol.* **2018**, *13*, 589–595.
- (19) Wen, Q.; Qian, W.; Nie, J.; Cao, A.; Ning, G.; Wang, Y.; Hu, L.; Zhang, Q.; Huang, J.; Wei, F. 100 mm Long, Semiconducting Triple-Walled Carbon Nanotubes. *Adv. Mater.* **2010**, *22*, 1867–1871.
- (20) Wen, Q.; Zhang, R.; Qian, W.; Wang, Y.; Tan, P.; Nie, J.; Wei, F. Growing 20 cm Long DWNTs/TWNTs at a Rapid Growth Rate of 80–90  $\mu\text{m}/\text{s}$ . *Chem. Mater.* **2010**, *22*, 1294–1296.
- (21) Rikanati, A.; Alon, U.; Shvarts, D. Vortex-Merger Statistical-Mechanics Model for the Late Time Self-Similar Evolution of the Kelvin–Helmholtz Instability. *Phys. Fluids* **2003**, *15*, 3776–3785.
- (22) Corcos, G. M.; Sherman, F. S. Vorticity Concentration and the Dynamics of Unstable Free Shear Layers. *J. Fluid Mech.* **1976**, *73*, 241–264.
- (23) Miles, J. W. On the Generation of Surface Waves by Shear Flows. Part 3. Kelvin–Helmholtz Instability. *J. Fluid Mech.* **1959**, *6*, 583.
- (24) Brown, G. L.; Roshko, A. On Density Effects and Large Structure in Turbulent Mixing Layers. *J. Fluid Mech.* **1974**, *64*, 775–816.
- (25) Luque, B.; Lacasa, L.; Ballesteros, F. J.; Robledo, A. Feigenbaum Graphs: A Complex Network Perspective of Chaos. *PLoS One* **2011**, *6*, e22410–e22411.
- (26) Araujo, P. T.; Pesce, P. B. C.; Dresselhaus, M. S.; Sato, K.; Saito, R.; Jorio, A. Resonance Raman Spectroscopy of the Radial Breathing Modes in Carbon Nanotubes. *Phys. E* **2010**, *42*, 1251–1261.
- (27) Liu, K.; Deslippe, J.; Xiao, F.; Capaz, R. B.; Hong, X.; Aloni, S.; Zettl, A.; Wang, W.; Bai, X.; Louie, S. G.; Wang, E.; Wang, F. An Atlas of Carbon Nanotube Optical Transitions. *Nat. Nanotechnol.* **2012**, *7*, 325–329.
- (28) Levshov, D. I.; Tran, H. N.; Paillet, M.; Arenal, R.; Than, X. T.; Zahab, A. A.; Yuzuk, Y. I.; Sauvajol, J. L.; Michel, T. Accurate Determination of the Chiral Indices of Individual Carbon Nanotubes by Combining Electron Diffraction and Resonant Raman Spectroscopy. *Carbon* **2017**, *114*, 141–159.
- (29) Dresselhaus, M. S.; Dresselhaus, G.; Jorio, A.; Souza Filho, A. G.; Saito, R. Raman Spectroscopy on Isolated Single Wall Carbon Nanotubes. *Carbon* **2002**, *40* (12), 2043–2061.
- (30) Ning, Z.; Chen, Q.; Wei, J.; Zhang, R.; Ye, L.; Wei, X.; Fu, M.; Guo, Y.; Bai, X.; Wei, F. Directly Correlating the Strain-Induced Electronic Property Change to the Chirality of Individual Single-Walled and Few-Walled Carbon Nanotubes. *Nanoscale* **2015**, *7*, 13116–13124.
- (31) Cao, Q.; Han, S.-J.; Tersoff, J.; Franklin, A. D.; Zhu, Y.; Zhang, Z.; Tulevski, G. S.; Tang, J.; Haensch, W. End-Bonded Contacts for Carbon Nanotube Transistors with Low, Size-Independent Resistance. *Science* **2015**, *350*, 68–72.
- (32) Liu, L.; Zhao, C.; Ding, L.; Peng, L.; Zhang, Z. Drain-Engineered Carbon-Nanotube-Film Field-Effect Transistors with High Performance and Ultra-Low Current Leakage. *Nano Res.* **2020**, *13*, 1875–1881.
- (33) Wang, N.; Tang, Z. K.; Li, G. D.; Chen, J. S. Single-Walled 4 Å Carbon Nanotube Arrays. *Nature* **2000**, *408*, 50–51.
- (34) Lenosky, T.; Gonze, X.; Teter, M.; Elser, V. Energetics of Negatively Curved Graphitic Carbon. *Nature* **1992**, *355*, 333–335.
- (35) Zhang, S.; Zhao, S.; Xia, M.; Zhang, E.; Xu, T. Ring Formation of Single-Walled Carbon Nanotubes: Competition between Conformation Energy and Entropy. *Phys. Rev. B: Condens. Matter Mater. Phys.* **2003**, *68*, 245419.
- (36) Zhong-Can, O.-Y.; Su, Z.-B.; Wang, C.-L. J. P. R. L. Coil Formation in Multishell Carbon Nanotubes: Competition between Curvature Elasticity and Interlayer Adhesion. *Phys. Rev. Lett.* **1997**, *78*, 4055.
- (37) Cornwell, C. F.; Wille, L. T. Elastic Properties of Single-Walled Carbon Nanotubes in Compression. *Solid State Commun.* **1997**, *101*, 555–558.
- (38) Tersoff, J.; Ruoff, R. S. Structural Properties of a Carbon-Nanotube Crystal. *Phys. Rev. Lett.* **1994**, *73*, 676–679.
- (39) Lin, S.; Liu, X.; Liu, J.; Yuk, H.; Loh, H.-C.; Parada, G. A.; Settens, C.; Song, J.; Masic, A.; McKinley, G. H. J. S. a. Anti-Fatigue-Fracture Hydrogels. *Sci. Adv.* **2019**, *5*, No. eaau8528.